

Radiogenomics of Glioblastoma: Machine Learning–based Classification of Molecular Characteristics by Using Multiparametric and Multiregional MR Imaging Features¹

Philipp Kickingereder, MD
David Bonekamp, MD
Martha Nowosielski, MD, PhD
Annekathrin Kratz, MD
Martin Sill, PhD
Sina Burth, MD
Antje Wick, MD
Oliver Eidel, MD
Heinz-Peter Schlemmer, MD, PhD
Alexander Radbruch, MD
Jürgen Debus, MD, PhD
Christel Herold-Mende, PhD
Andreas Unterberg, MD
David Jones, PhD
Stefan Pfister, MD
For the Group²

Purpose:

To evaluate the association of multiparametric and multiregional magnetic resonance (MR) imaging features with key molecular characteristics in patients with newly diagnosed glioblastoma.

Materials and Methods:

Retrospective data evaluation was approved by the local ethics committee, and the requirement to obtain informed consent was waived. Preoperative MR imaging features were correlated with key molecular characteristics within a single-institution cohort of 152 patients with newly diagnosed glioblastoma. Preoperative MR imaging features ($n = 31$) included multiparametric (anatomic and diffusion-, perfusion-, and susceptibility-weighted images) and multiregional (contrast-enhancing regions and hyperintense regions at nonenhanced fluid-attenuated inversion recovery imaging) information with histogram quantification of tumor volumes, volume ratios, apparent diffusion coefficients, cerebral blood flow, cerebral blood volume, and intratumoral susceptibility signals. Molecular characteristics determined included global DNA methylation subgroups (eg, mesenchymal, *RTK I* “*PGFRA*,” *RTK II* “classic”), *MGMT* promoter methylation status, and hallmark copy number variations (*EGFR*, *PDGFRA*, *MDM4*, and *CDK4* amplification; *PTEN*, *CDKN2A*, *NF1*, and *RB1* loss). Univariate analyses (voxel-lesion symptom mapping for tumor location, Wilcoxon test for all other MR imaging features) and machine learning models were applied to study the strength of association and discriminative value of MR imaging features for predicting underlying molecular characteristics.

Results:

There was no tumor location predilection for any of the assessed molecular parameters (permutation-adjusted $P > .05$). Univariate imaging parameter associations were noted for *EGFR* amplification and *CDKN2A* loss, with both demonstrating increased Gaussian-normalized relative cerebral blood volume and Gaussian-normalized relative cerebral blood flow values (area under the receiver operating characteristics curve: 63%–69%, false discovery rate-adjusted $P < .05$). Subjecting all MR imaging features to machine learning–based classification enabled prediction of *EGFR* amplification status and the *RTK II* glioblastoma subgroup with a moderate, yet significantly greater, accuracy (63% for *EGFR* [$P < .01$], 61% for *RTK II* [$P = .01$]) than prediction by chance; prediction accuracy for all other molecular parameters was not significant.

Conclusion:

The authors found associations between established MR imaging features and molecular characteristics, although not of sufficient strength to enable generation of machine learning classification models for reliable and clinically meaningful prediction of molecular characteristics in patients with glioblastoma.

©RSNA, 2016

Online supplemental material is available for this article.

¹ From the Department of Neuroradiology, University of Heidelberg Medical Center, Im Neuenheimer Feld 400, 69120 Heidelberg, Germany (P.K.). Received June 16, 2016; revision requested July 5; revision received August 11; final version accepted August 16. Address correspondence to P.K. (e-mail: philipp.kickingereder@med.uni-heidelberg.de).

² The complete list of authors and affiliations is at the end of this article.

S.B. is supported by a grant from German Cancer Aid (111583). P.K. is a fellow of the Medical Faculty Heidelberg Postdoc Program.

©RSNA, 2016

Magnetic resonance (MR) imaging is routinely used in the diagnosis, prognostic assessment,

Advances in Knowledge

- Univariate associations between certain MR imaging features and key molecular parameters in patients with glioblastoma exist (specifically for tumors with epidermal growth factor receptor [*EGFR*] amplification or *CDKN2A* loss, with both demonstrating increased Gaussian-normalized relative cerebral blood volume and Gaussian-normalized relative cerebral blood flow values; false discovery rate-adjusted $P < .05$); however, the predictive performance is moderate (area under the receiver operating characteristic curve, 63%–69%), thus questioning the ability of single imaging parameters to help predict key molecular parameters.
- There was no significant tumor location predilection (assessed on a voxel-by-voxel basis) for any of the evaluated molecular parameters (global DNA methylation subgroups [eg, mesenchymal, *RTK I* “*PGFRA*,” *RTK II* “classic”]; *MGMT* promoter methylation; *EGFR*, *PDGFRA*, *MDM4* and *CDK4* amplification; *PTEN*, *CDKN2A*, *NF1*, and *RB1* loss; permutation-adjusted $P > .05$ for all).
- Machine learning-based classification integrating the information from all evaluated MR imaging features ($n = 31$) showed that *EGFR* amplification status and *RTK II* subgroup prediction were the only molecular parameters that could be predicted with a moderate, yet significantly greater, accuracy (63% for *EGFR* [$P < .01$] and 61% for *RTK II* [$P = .01$]) than prediction by chance, whereas prediction accuracy for all other molecular parameters was not significant ($P > .05$ for all).

and clinical management of patients with glioblastoma (1,2). Noninvasive MR imaging enables the assessment of the tumor in its entirety and helps define its interaction with the local environment (3). In its ability to enable the extraction of structural, physiologic, and functional information, MR imaging allows for multidimensional in vivo characterization of glioblastoma (3,4). However, most of these noninvasive descriptors remain unspecific at a molecular level. To overcome this limitation, a relatively new discipline called “radiogenomics” has recently been established to study the relationship between noninvasive imaging features and corresponding molecular characteristics (5–8). To date, several explorative studies have demonstrated associations between molecular characteristics and imaging features, including tumor location (9), tumor volume (10,11), enhancement (3,12), invasiveness (13), edema (7,14), and diffusion restriction (5,15). Recently, distinct imaging clusters were shown to map to a unique set of molecular signaling pathways associated with different patient survival (16). Although tissue for histologic analysis is available for nearly all glioblastoma at diagnosis, repeat surgery and tissue sampling is rarely performed at recurrence (17). Moreover, divergent recurrences that share only a few genetic alterations with the primary tumor and originate from cells that branched off early during tumorigenesis (18) may compromise the value of molecular information obtained from initial surgery in the setting of tumor recurrence. Consequently, establishing molecular feature predictions by using a radiogenomics approach may enable follow up of patients under a sufficient or insufficient therapy longitudinally and adaptation of treatment and thereby circumvent the intrinsic challenge of multiple biopsies in a tumor location in the brain.

In this study, we explored the association of established preoperative MR imaging parameters with key molecular features from the initial surgery within a homogeneous single-institution cohort of 152 consecutive

patients with newly diagnosed glioblastoma. MR imaging parameters were extracted in a semi-automated and quantitative fashion and included multiparametric and multiregional information from the three-dimensional tumor volumes. Molecular features determined with a DNA methylation microarray (Infinium HumanMethylation450 BeadChip kit; Illumina, San Diego, Calif) included previously established global DNA methylation subgroups as well as O6-methylguanine-DNA-methyltransferase (*MGMT*) promoter methylation status (19) and hallmark copy number variation (CNV) of glioblastoma (20,21). The overarching objective of this study was to identify imaging signatures that help predict single prognostic or predictive molecular biomarkers or epigenomic clusters by means of multidimensional MR imaging features. The specific aims of this study were to (a) evaluate univariate associations in an explorative analysis and (b) subsequently create predictive machine learning-based classification models

Published online before print

10.1148/radiol.2016161382 Content codes: **MR** **NR**

Radiology 2016; 281:907–918

Abbreviations:

ADC = apparent diffusion coefficient

CNV = copy number variation

FLAIR = fluid-attenuated inversion recovery

nADC = Gaussian-normalized ADC

nrCBF = Gaussian-normalized relative cerebral blood flow

nrCBV = Gaussian-normalized relative cerebral blood volume

Author contributions:

Guarantors of integrity of entire study, P.K., D.C.; study concepts/study design or data acquisition or data analysis/interpretation, all authors; manuscript drafting or manuscript revision for important intellectual content, all authors; manuscript final version approval, all authors; agrees to ensure any questions related to the work are appropriately resolved, all authors; literature research, P.K., D.B., A.K., S.B., A.W., H.P.S., A.R., C.H.M., A.U., M.B., D.C.; clinical studies, P.K., D.B., M.N., S.B., A.W., O.E., A.R., J.D., C.H.M., A.U., W.W.; experimental studies, P.K., A.K., A.W., O.E., C.H.M., D.J., S.P., A.v.D., D.C.; statistical analysis, P.K., D.B., M.S., A.W., C.H.M., A.U., M.B.; and manuscript editing, P.K., D.B., M.N., A.K., S.B., O.E., H.P.S., A.R., J.D., C.H.M., A.U., D.J., W.W., A.v.D., M.B., D.C.

Conflicts of interest are listed at the end of this article.

that enable evaluation of the performance of the multivariate and multidimensional imaging appearance for predicting underlying key molecular characteristics.

Materials and Methods

Retrospective evaluation of imaging data was approved by the local ethics committee of the University of Heidelberg (ethics approval number: S-320/2012), and the requirement to obtain informed consent was waived. DNA methylation analysis was performed as part of the National Center for Tumor Diseases Precision Oncology Program of the Heidelberg Center for Personalized Oncology. All patients with newly diagnosed brain tumor at the University of Heidelberg Medical Center (Heidelberg, Germany) between August 2009 and May 2016 and for whom DNA methylation microarray data from tissue specimens obtained at the initial surgery were available (Infinium HumanMethylation450 array) were screened. The DNA methylation microarray data were obtained from patients undergoing surgical resection or biopsy at the Department of Neurosurgery, University of Heidelberg Medical Center, and gathered according to the research procedures approved by the institutional review board at the Medical Faculty Heidelberg; written consent was obtained from each patient. We selected those patients with histologically confirmed glioblastoma and in whom corresponding pretreatment MR images were obtained before surgery with an identical sequence protocol, including T1-weighted three-dimensional magnetization-prepared rapid acquisition gradient-echo imaging performed before and after contrast material administration, fluid-attenuated inversion recovery (FLAIR) imaging, diffusion-weighted imaging, dynamic susceptibility-weighted contrast-enhanced imaging, and precontrast susceptibility-weighted imaging. Patients were excluded if the MR imaging data were of insufficient quality due to motion artifacts or poor

contrast material injection ($n = 7$). A total of 152 patients met the outlined inclusion and exclusion criteria and served as the final cohort for the present study.

DNA Methylation Profiling

The Infinium HumanMethylation450 array was used to obtain genome-wide assessment of DNA methylation according to the manufacturer's instructions at the Genomics and Proteomics Core Facility of the German Cancer Research Center and as described previously (21). Data were filtered according to the following criteria: removal of probes targeting the X and Y chromosomes ($n = 11551$), removal of probes containing a single nucleotide polymorphism (dbSNP132 Common) within five base pairs of and including the targeted CpG site ($n = 24536$), and removal of probes not mapping uniquely to the human reference genome (hg19), allowing for one mismatch ($n = 9993$). In total, 438370 probes were kept for analysis. Each patient was assigned to one of the previously defined glioblastoma subgroups (mesenchymal [MES], *RTK I* [platelet-derived growth factor receptor alpha, "PDGFRA"], *RTK II* ["classic"], isocitrate dehydrogenase [*IDH*], *K27*, *G34*) on the basis of the global DNA methylation pattern (21). Briefly, as described previously, a random forest algorithm compared each included case with a brain tumor DNA methylation profile reference bank consisting of more than 2000 brain tumor cases to obtain the glioblastoma subgroup predictions (22,23). *MGMT* promoter methylation status (methylated vs unmethylated) was predicted from the Infinium HumanMethylation450 array data as described previously (by using the *mgmtstp27* package) (24). For a subset of samples where the *mgmtstp27* package failed to predict the *MGMT* promoter methylation status (13 of 20 samples) additional *MGMT* pyrosequencing was performed as described previously (25). CNV analysis based on the Infinium HumanMethylation450 array data included assessment of epidermal growth factor receptor (*EGFR*, amplified vs nonamplified), *PDGFRA*

(amplified vs nonamplified), cyclin-dependent kinase 4 (*CDK4*, amplified vs nonamplified), and *MDM4* (amplified vs nonamplified) and loss of phosphatase and tensin homolog (*PTEN*, loss vs balanced), cyclin-dependent kinase inhibitor 2A (*CDKN2A*, loss vs balanced), neurofibromin 1 (*NF1*, loss vs balanced), and retinoblastoma 1 (*RBI*, loss vs balanced). The array data of the present study have been deposited in National Center for Biotechnology Information's Gene Expression Omnibus (<http://www.ncbi.nlm.nih.gov/geo>) and are accessible through Gene Expression Omnibus Series accession number GSE85539.

MR Imaging and Image Postprocessing

Images were acquired during routine clinical work-up by using a 3.0-T MR imaging system (Magnetom Verio/Trio TIM; Siemens Healthcare, Erlangen, Germany) and included pre- and postcontrast magnetization-prepared rapid acquisition gradient-echo images, FLAIR images, diffusion-weighted images (with apparent diffusion coefficient [ADC] maps and b values of 1200 sec/mm²), dynamic susceptibility-weighted contrast-enhanced MR images, and precontrast susceptibility-weighted images. Details on MR imaging acquisition parameters and the complete postprocessing workflow (performed by P.K., a radiology resident with 4 years of experience, and D.B., a board-certified radiologist and neuroradiologist with 15 years of experience in image processing) are outlined in the Appendix E1, section S1 (online). Briefly, for each patient a total of 31 imaging parameters were calculated from contrast-enhancing tumor volumes, necrotic tumor volumes, hyperintense tumor volumes on FLAIR images ("nonenhancing and edema" regions, excluding voxels within the contrast-enhancing and necrotic segmentation), and complete tumor volumes (contrast enhancing + nonenhancing and edema + necrotic tumor volumes, subsequently referred to as "total" volumes) and included quantification of tumor volumes, volume ratios, and histogram quantification of

Table 1

Description of the Extracted Imaging Parameters

Imaging Parameter	Description
Volume (TOTAL)	Complete tumor volume (contrast-enhancing volume + hyperintense volume on FLAIR images + necrotic volume)
Volume (NEC)	Necrotic tumor volume
Volume (NE_EDEMA)	Hyperintense volume on FLAIR images (excluding voxels within the contrast-enhancing and necrotic tumor volume)
Volume (CENEC)	Contrast-enhancing + necrotic tumor volume
Volume (CE)	Contrast-enhancing tumor volume
Ratio NE_EDEMA-to-TOTAL	Ratio of hyperintense tumor volume on FLAIR images to complete tumor volume
Ratio NEC-to-TOTAL	Ratio of necrotic tumor volume to complete tumor volume
Ratio CE-to-TOTAL	Ratio of contrast-enhancing tumor volume to complete tumor volume
Ratio NE_EDEMA-to-CE	Ratio of hyperintense volume on FLAIR images to contrast-enhancing tumor volume
nrCBV prc95 (TOTAL)	95th percentile of the nrCBV from the complete tumor volume
nrCBV prc95 (NE_EDEMA)	95th percentile of the nrCBV from the hyperintense volume on FLAIR images
nrCBV prc95 (CE)	95th percentile of the nrCBV from the contrast-enhancing tumor volume
nrCBV mean (TOTAL)	Mean nrCBV from the complete tumor volume
nrCBV mean (NE_EDEMA)	Mean nrCBV from the hyperintense volume on FLAIR images
nrCBV mean (CE)	Mean nrCBV from the contrast-enhancing tumor volume
nrCBF prc95 (TOTAL)	95th percentile of the nrCBF from the complete tumor volume
nrCBF prc95 (NE_EDEMA)	95th percentile of the nrCBF from the hyperintense volume on FLAIR images
nrCBF prc95 (CE)	95th percentile of the nrCBF from the contrast-enhancing tumor flow
nrCBF mean (TOTAL)	Mean nrCBF from the complete tumor volume
nrCBF mean (NE_EDEMA)	Mean nrCBF from the hyperintense volume on FLAIR images
nrCBF mean (CE)	Mean nrCBF from the contrast-enhancing tumor volume
nADC prc5 (TOTAL)	5th percentile of the nADC from the complete tumor volume
nADC prc5 (NE_EDEMA)	5th percentile of the nADC from the hyperintense volume on FLAIR images
nADC prc5 (CE)	5th percentile of the nADC from the contrast-enhancing tumor volume
nADC mean (TOTAL)	Mean nADC from the complete tumor volume
nADC mean (NE_EDEMA)	Mean nADC from the hyperintense volume on FLAIR images
nADC mean (CE)	Mean nADC from the contrast-enhancing tumor volume
SWI-h (TOTAL)	Fraction of SWI hypointensities within the complete tumor volume
SWI-h (NE_EDEMA)	Fraction of SWI hypointensities within the hyperintense volume on FLAIR images
SWI-h (CENEC)	Fraction of SWI hypointensities within the contrast-enhancing + necrotic tumor volume
SWI-h (CE)	Fraction of SWI hypointensities within the contrast-enhancing tumor volume

Note.—SWI =susceptibility-weighted imaging.

Gaussian-normalized ADC (nADC), Gaussian-normalized relative cerebral blood flow and volume (nrCBF and nrCBV, respectively), and intratumoral susceptibility signals (see Table 1 for a detailed listing).

Statistical Analysis

We examined all molecular parameters for statistically significant differences regarding tumor location on a voxel-by-voxel basis by employing a voxel-based

lesion symptom mapping approach implemented in Matlab (MathWorks, Natick, Mass) (detailed information is provided in Appendix E1, section S2 [online]).

Subsequent analysis was performed (P.K. and M.S., a biostatistician with 8 years of experience in computational biology) by using software (R, version 3.3.1; R Foundation for Statistical Computing, Vienna, Austria). Univariate association of each imaging parameter

Table 2

Baseline Epidemiologic, Histologic, and Molecular Characteristics in 152 Patients

Parameter	Value
Sex	
M	84
F	68
Median age (y)*	63 (55–71)
Median interval between MR imaging and surgery (d)*	3 (1–6)
Molecular diagnosis	
GB: <i>MES</i>	50 (33)
GB: <i>RTK I</i> “ <i>PDGFRA</i> ”	22 (14)
GB: <i>RTK II</i> “classic”	74 (49)
GB: <i>IDH</i>	2 (1)
GB: <i>G34</i>	2 (1)
NA	2 (1)
<i>MGMT</i> promoter methylation status	
Methylated	68 (45)
Unmethylated	77 (51)
NA	7 (5)
<i>EGFR</i> status	
Amplified	77 (51)
Nonamplified	75 (49)
<i>PDGFRA</i> status	
Amplified	12 (8)
Nonamplified	140 (92)
<i>MDM4</i> status	
Amplified	15 (10)
Nonamplified	136 (89)
NA	1 (1)
<i>CDK4</i> status	
Amplified	17 (11)
Nonamplified	135 (89)
<i>PTEN</i> status	
Loss	132 (87)
Balanced	18 (12)
NA	2 (1)
<i>CDKN2A</i> status	
Loss	118 (78)
Balanced	33 (22)
NA	1 (1)
<i>NF1</i> status	
Loss	26 (17)
Balanced	121 (80)
NA	5 (3)
<i>RB1</i> status	
Loss	46 (30)
Balanced	101 (66)
NA	5 (3)

Note.—Except where indicated, data are numbers of patients, with percentages in parentheses. GB = glioblastoma, NA = not applicable, status cannot be classified.

* Numbers in parentheses are the interquartile range.

Figure 1

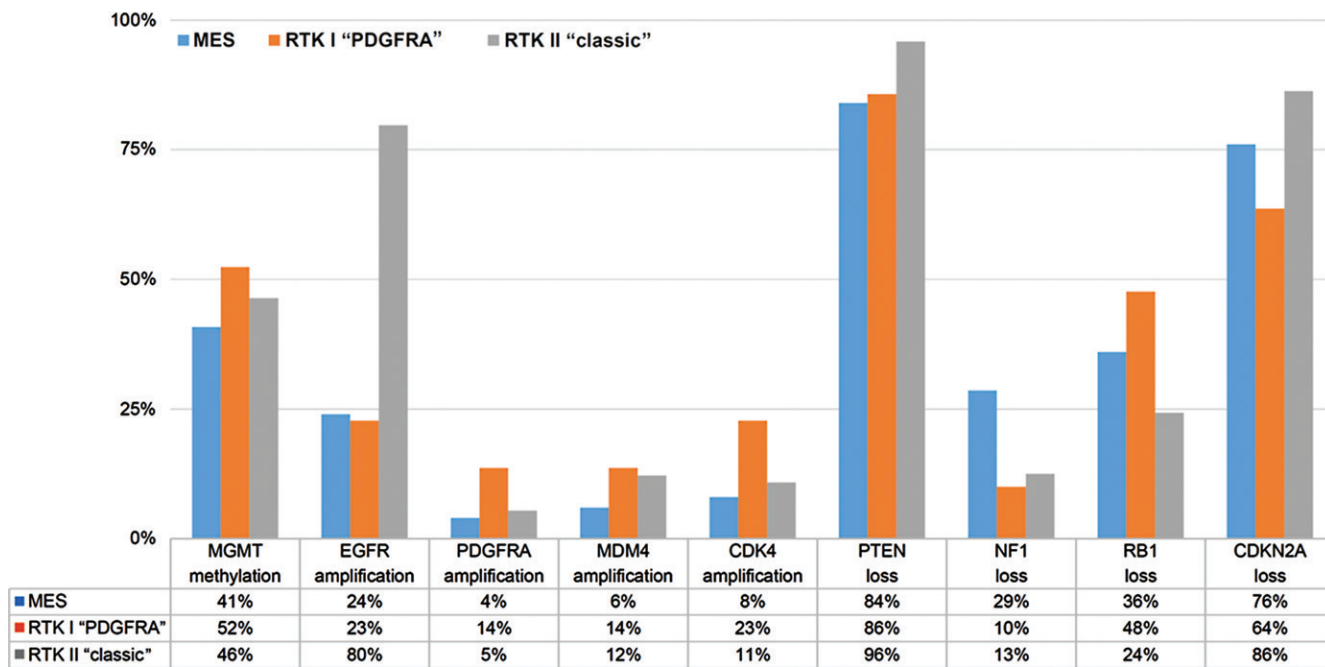


Figure 1: Bar chart shows distribution of molecular parameters among DNA methylation subgroups *RTK I*, *RTK II*, and *MES* (other subgroups not shown).

($n = 31$) with molecular parameters (glioblastoma subgroups [*MES* vs non-*MES*, *RTK I* vs non-*RTK I*, *RTK II* vs non-*RTK II*], *MGMT* [methylated vs unmethylated], *EGFR* [amplified vs nonamplified], *PDGFRA* [amplified vs nonamplified], *MDM4* [amplified vs nonamplified], *CDK4* [amplified vs nonamplified], *PTEN* [loss vs balanced], *CDKN2A* [loss vs balanced], *NF1* [loss vs balanced], *RB1* [loss vs balanced]) was determined with the Wilcoxon rank-sum test (wilcox.test function of the statistical package). *P* values generated for each molecular parameter with the Wilcoxon rank-sum test were corrected for multiple comparisons by means of false discovery rate adjustment by using the Benjamini-Hochberg procedure (p.adjust function of the statistical package). The predictive performance of each imaging parameter was quantified by calculating the area under the receiver operating characteristic curve (roc function of the pROC package).

To examine the value of combining multiple parameters to arrive at

stronger prediction models, we subsequently used advanced statistical methods to study multiparametric image performance by training a range of machine learning-based classification models that aim to construct prediction models for each of the analyzed molecular parameters by integrating the information from all evaluated MR imaging features. These machine learning algorithms aim to produce strong prediction models in the form of an ensemble of (univariate) prediction models, where some of the included parameters may be weak in the univariate setting but contribute advantageously to the overall performance of the combined model. All imaging features were z-score normalized (ie, transformed to a mean of 0 and a standard deviation equal to 1) and then subjected to machine learning algorithms (by using the caret package [26]), which aim to construct prediction models for each of the analyzed molecular parameters by integrating the information from all imaging features. Model training was performed with three popular

machine learning methods for binary classification problems and included (a) stochastic gradient boosting machine, (b) random forest, and (c) penalized logistic regression classifiers (a detailed explanation is given in Appendix E1, section S3 [online]).

The performance of each machine learning classifier was assessed on the basis of a 10-fold cross-validation resampling procedure. We also used subsampling during resampling to resolve disparity in the frequencies of the observed classes for each molecular parameter (eg, *CDKN2A* demonstrated a 3.5:1 imbalance with *CDKN2A* loss in 78% of patients and balanced *CDKN2A* in 22% of patients [Table 2]), which can have a negative effect on model fitting. Specifically, each machine learning model was trained (a) without subsampling, (b) with random oversampling examples, and (c) with synthetic minority oversampling technique, which downsamples the majority class and synthesizes new data points in the minority class. Finally, the held-out predictions of each molecular parameter in each of

the 10 resampling iterations were used to calculate the accuracy, area under the receiver operating characteristic curve, sensitivity, specificity, no-information rate (largest class percentage for each molecular parameter; ie, the prediction or accuracy by chance), and a hypothesis test (with the `binom.test` function) was used to evaluate whether the accuracy rate is greater than the no-information rate. $P < .05$ was considered indicative of a statistically significant difference.

Results

Baseline epidemiologic and molecular characteristics are shown in Table 2. In brief, the median interval from MR imaging to surgery was 3 days (interquartile range, 1–6 days). The most frequent molecular glioblastoma subtype was the *RTK II* (classic) subtype (49%), followed by the mesenchymal subtype (33%) and the *RTK I* (*PDGFRA*) subtype (14%). *MGMT* promoter methylation was present in 45% of patients, and *EGFR* amplification was present in 51%. A detailed listing of all assessed CNVs (*EGFR*, *PTEN*, *CDKN2A*, *NF1*, *PDGFRA*, *MDM4*, *CDK4*, *RB1*) is shown in Table 2. Figure 1 shows the distribution of the assessed CNVs and *MGMT* grouped according to the different molecular glioblastoma subtypes.

Voxel-based lesion symptom mapping analysis demonstrated no significant tumor location predilection for any of the assessed molecular parameters (permutation-adjusted $P > .05$ for each; detailed results are provided in Appendix E1, section S2 [online]).

Univariate association of each imaging parameter with the corresponding molecular parameter (Appendix E1, section S4 [online]) demonstrated a significant relationship between (a) *EGFR* amplification with increased nrCBV and nrCBF within the contrast-enhanced and total tumor volumes and (b) *CDKN2A* loss with increased nrCBV and nrCBF within the contrast-enhanced tumor volume (the predictive performance of these parameters, as assessed with the area under

Table 3

Performance Metrics from Machine Learning–based Classification of Molecular Parameters

Molecular Parameter, Method, and Subsampling	AUC (%)	Accuracy (%)	95% CI (%)	No-Information Rate (%)*	<i>P</i> Value†	Sensitivity (%)	Specificity (%)
Methylation subgroup (MES vs non-MES)							
PLR							
None	52	55	47, 63	67	.99	16	75
SMOTE	53	55	46, 63	67	.99	38	63
ROSE	53	47	39, 55	67	.99	38	51
RF							
None	46	65	57, 73	67	.73	12	91
SMOTE	46	59	50, 67	67	.99	46	65
ROSE	46	46	38, 54	67	.99	68	35
sGBM							
None	53	59	50, 67	67	.99	22	77
SMOTE	57	59	50, 67	67	.99	46	65
ROSE	51	48	40, 56	67	.99	62	41
Methylation subgroup (RTK I vs non-RTK I)							
PLR							
None	54	85	78, 90	86	.64	18	96
SMOTE	61	66	58, 74	86	.99	50	69
ROSE	51	53	44, 61	86	.99	50	53
RF							
None	46	86	80, 91	86	.47	9	99
SMOTE	46	75	67, 82	86	.99	41	81
ROSE	46	26	20, 34	86	.99	91	15
sGBM							
None	52	85	78, 90	86	.64	0	99
SMOTE	60	73	65, 80	86	.99	32	80
ROSE	56	24	17, 31	86	.99	96	12
Methylation subgroup (RTK II vs non-RTK II)							
PLR							
None	58	58	50, 66	51	.06	50	65
SMOTE	59	56	48, 64	51	.15	39	72
ROSE	52	53	45, 61	51	.34	55	51
RF							
None‡	53	61	53, 69	51	.01	53	69
SMOTE	53	53	45, 61	51	.34	62	45
ROSE	53	53	44, 61	51	.40	41	64
sGBM							
None	58	54	46, 62	51	.29	49	59
SMOTE‡	62	61	53, 69	51	.01	62	60
ROSE	52	53	44, 61	51	.40	41	64
MGMT promoter (methylated vs unmethylated)							
PLR							
None	60	59	51, 67	53	.08	57	61
SMOTE	59	58	50, 66	53	.14	56	60
ROSE	54	52	44, 61	53	.60	40	64

Table 3 (continues)

Table 3 (continued)

Performance Metrics from Machine Learning–based Classification of Molecular Parameters

Molecular Parameter, Method, and Subsampling	AUC (%)	Accuracy (%)	95% CI (%)	No-Information Rate (%)*	P Value†	Sensitivity (%)	Specificity (%)
RF							
None	58	52	44, 61	53	.60	49	56
SMOTE	58	57	49, 65	53	.18	63	52
ROSE	58	55	47, 63	53	.34	49	61
sGBM							
None	61	56	47, 64	53	.28	49	62
SMOTE	57	56	47, 64	53	.28	44	66
ROSE	57	52	44, 61	53	.60	38	65
EGFR (amplified vs nonamplified)							
PLR							
None‡	64	59	50, 67	51	.03	62	55
SMOTE‡	67	63	54, 70	51	.00	71	53
ROSE‡	63	61	52, 68	51	.01	66	55
RF							
None‡	51	59	51, 67	51	.02	64	55
SMOTE‡	51	62	54, 70	51	.00	55	69
ROSE	51	56	48, 64	51	.11	70	41
sGBM							
None‡	67	60	52, 68	51	.01	62	57
SMOTE‡	71	62	54, 70	51	.00	69	55
ROSE	61	57	48, 65	51	.08	94	19
CDK4 (amplified vs nonamplified)							
PLR							
None	56	88	81, 92	89	.75	0	99
SMOTE	48	67	59, 75	89	.99	35	71
ROSE	55	62	54, 70	89	.99	24	67
RF							
None	54	88	81, 92	89	.75	0	99
SMOTE	54	62	54, 70	89	.99	6	69
ROSE	54	52	44, 60	89	.99	47	53
sGBM							
None	45	87	80, 92	89	.82	0	98
SMOTE	51	64	56, 71	89	.99	24	69
ROSE	53	57	48, 65	89	.99	29	60
PDGFRA (amplified vs nonamplified)							
PLR							
None	59	85	78, 90	92	.99	8	91
SMOTE	61	72	64, 79	92	.99	33	75
ROSE	74	55	47, 63	92	.99	8	59
RF							
None	54	92	87, 96	92	.58	8	99
SMOTE	54	75	67, 82	92	.99	17	80
ROSE	54	43	35, 51	92	.99	58	41
sGBM							
None	56	91	86, 95	92	.69	0	99
SMOTE	63	77	70, 83	92	.99	8	83
ROSE	47	47	39, 56	92	.99	58	46

Table 3 (continues)

the receiver operating characteristic curve, ranged from 63% to 69%; false discovery rate–adjusted $P < .05$). Further potential associations were noted (*PTEN* loss: higher nrCBV and nrCBF in the contrast-enhanced and total tumor volumes; *CDKN2A* loss: higher nrCBV and nrCBF in the total tumor volume; *CDK4* amplification: higher nADC in the contrast-enhanced and total tumor volumes; *MGMT* methylation: higher ratio of contrast-enhancing tumor volume to complete tumor volume, higher nrCBV and nrCBF in the contrast-enhanced and total tumor volumes; *MES* subgroup: lower nrCBV and nrCBF in the nonenhanced edema tumor volume; *RTK I* subgroup: lower nrCBF in the contrast-enhanced tumor volume; *RTK II* subgroup: higher nrCBV in the contrast-enhanced and total tumor volumes); however, none of these associations were of sufficient strength to retain significance after false discovery rate adjustment.

The performance of machine learning prediction models for molecular parameters is summarized in Table 3. *EGFR* amplification status and *RTK II* subgroup prediction were the only molecular parameters that could be predicted with an accuracy (59%–63% for *EGFR* and 61% for *RTK II*) that was significantly greater than the prediction by chance (51% for both *EGFR* and *RTK II*) ($P = .00$ – $.03$ for *EGFR* and $P = .01$ for *RTK II*). The highest accuracy for predicting *EGFR* amplification status (63%) was obtained with a penalized logistic regression model with synthetic minority oversampling technique subsampling; the highest accuracy for *RTK II* subgroup prediction (61%) was obtained with a stochastic gradient boosting model with synthetic minority oversampling technique subsampling and a random forest model without subsampling (Appendix E1, section S5 [online] shows the variable importance plots with the relative importance of each imaging parameter in these models). Apart from that, none of the machine learning–based classification models (regardless of whether stochastic

gradient-boosting machines, random forest, or penalized logistic regression models with or without subsampling) enabled prediction of any of the remaining molecular parameters (molecular glioblastoma subgroups [*MES* vs non-*MES*, *RTK I* vs non-*RTK I*], *MGMT* promoter methylation and the assessed CNVs [*PTEN* loss, *CDKN2A* loss, *NF1* loss, *PDGFRA* amplification, *MDM4* amplification, *CDK4* amplification, *RB1* loss]) on the basis of the combination of the extracted imaging parameters with an accuracy greater than the prediction by chance ($P > .05$ for all models). Of note is that the chosen machine learning models yield robust classification results despite multicollinearity, that is, the presence of correlated imaging features (Pearson correlation coefficient >0.75 for 19 of the 31 imaging features; Figure 2 shows a detailed correlation matrix). This was confirmed by subjecting only those imaging features with a Pearson correlation coefficient of 0.75 or less (ie, 12 of the 31 features) to the machine learning algorithms, thereby demonstrating identical results with *EGFR* and *RTK II* as the only molecular parameters that could be predicted with an accuracy greater than the prediction by chance (maximum accuracy of 62% for *EGFR* and 59% for *RTK II*; $P < .05$ for each; data not shown).

Discussion

In our well-characterized study cohort, we found that associations between certain imaging and molecular parameters exist, although only to a limited extent. We found moderate univariate associations of increased nrCBV and nrCBF values in patients with *EGFR* amplification and *CDKN2A* loss, with a performance that, however, questions the ability of a single imaging parameter to help predict key molecular parameters. The integrative performance of all imaging parameters assessed with machine learning-based models showed that *EGFR* amplification status and *RTK II* subtype classification could be predicted with moderate,

Table 3 (continued)

Performance Metrics from Machine Learning–based Classification of Molecular Parameters

Molecular Parameter, Method, and Subsampling	AUC (%)	Accuracy (%)	95% CI (%)	No-Information Rate (%)*	P Value†	Sensitivity (%)	Specificity (%)
<i>MDM4</i> (amplified vs nonamplified)							
PLR							
None	50	89	83, 94	90	.67	0	99
SMOTE	59	66	58, 74	90	.99	53	68
ROSE	55	49	41, 57	90	.99	47	49
RF							
None	59	89	83, 93	90	.76	0	99
SMOTE	59	76	68, 82	90	.99	27	81
ROSE	59	43	35, 51	90	.99	60	41
sGBM							
None	56	89	83, 94	90	.67	0	99
SMOTE	64	77	69, 83	90	.99	33	82
ROSE	54	47	39, 55	90	.99	53	46
<i>CDKN2A</i> (balanced vs loss)							
PLR							
None	65	76	69, 83	78	.76	0	98
SMOTE	59	64	56, 72	78	.99	42	70
ROSE	56	54	46, 62	78	.99	49	56
RF							
None	52	78	70, 84	78	.62	3	98
SMOTE	52	70	62, 77	78	.99	39	79
ROSE	52	67	59, 74	78	.99	42	74
sGBM							
None	61	74	66, 81	78	.90	6	93
SMOTE	59	61	53, 69	78	.99	39	67
ROSE	59	62	54, 70	78	.99	39	69
<i>PTEN</i> (balanced vs loss)							
PLR							
None	80	87	80, 92	88	.74	39	93
SMOTE	82	81	73, 87	88	.99	56	84
ROSE	75	76	68, 83	88	.99	56	79
RF							
None	56	88	82, 93	88	.56	0	100
SMOTE	56	80	73, 86	88	.99	39	86
ROSE	56	48	40, 56	88	.99	89	42
sGBM							
None	69	87	80, 92	88	.74	6	98
SMOTE	78	79	71, 85	88	.99	56	82
ROSE	70	33	26, 42	88	.99	83	27
<i>RB1</i> (balanced vs loss)							
PLR							
None	49	65	57, 73	69	.84	94	2
SMOTE	51	57	49, 65	69	.99	69	30
ROSE	49	50	41, 58	69	.99	54	41
RF							
None	58	59	51, 67	69	.99	84	4
SMOTE	58	52	43, 60	69	.99	63	26
ROSE	58	42	34, 51	69	.99	23	85

Table 3 (continues)

Table 3 (continued)

Performance Metrics from Machine Learning–based Classification of Molecular Parameters

Molecular Parameter, Method, and Subsampling	AUC (%)	Accuracy (%)	95% CI (%)	No-Information Rate (%)*	P Value†	Sensitivity (%)	Specificity (%)
sGBM							
None	52	62	54, 70	69	.97	84	13
SMOTE	54	50	42, 59	69	.99	59	30
ROSE	53	50	41, 58	69	.99	42	67
NF1 (balanced vs loss)							
PLR							
None	59	74	66, 80	82	.99	84	23
SMOTE	61	69	61, 76	82	.99	74	46
ROSE	52	51	43, 59	82	.99	53	42
RF							
None	60	82	75, 88	82	.55	100	0
SMOTE	60	74	66, 81	82	.99	83	35
ROSE	60	38	30, 47	82	.99	31	73
sGBM							
None	53	82	74, 88	82	.64	98	8
SMOTE	62	71	63, 79	82	.99	79	35
ROSE	50	40	32, 48	82	.99	35	62

Note.—Performance metrics are from hold-out samples (based on 10-fold cross-validation) and are based on all 31 imaging parameters. AUC = area under the receiver operating characteristic curve, CI = confidence interval, PLR = lasso and elastic net regularized generalized linear model, RF = random forest, ROSE = random oversampling examples, sGBM = stochastic gradient boosting machines, SMOTE = synthetic minority oversampling technique.

* Largest class percentage of each molecular parameter (ie, the prediction by chance).

† Obtained with the one-sided binomial test evaluating whether the model accuracy is greater than the no-information rate.

‡ Statistically significant predictions.

yet significant, accuracy. None of the other molecular parameters showed a univariate association with any of the assessed imaging features, nor could they be predicted on the basis of multiparametric image feature–based machine learning models with an accuracy greater than that of prediction by chance. In addition, voxel-based lesion symptom mapping analysis showed no significant tumor location predilection for any of the assessed molecular parameters in our study cohort.

Our finding of elevated nrCBV and nrCBF—which reflects increased intratumoral angiogenesis (27)—in tumors with *EGFR* amplification may correspond to the promotion of angiogenesis in a subset of patients with *EGFR* amplification (28). *EGFR* amplifications are present in approximately 50% of glioblastoma, and about half of them also harbor a constitutively activated mutated *EGFRvIII* isoform

(a mutation that is usually confined to *EGFR*-amplified tumors and only rarely present in tumors without *EGFR* amplification) (29,30), which promotes angiogenesis via distinct signaling pathways (28). Our results may therefore be in line with those from a recent study by Arevalo-Perez et al (31), who reported elevated relative plasma volume (from dynamic contrast-enhanced MR imaging) in patients with *EGFRvIII*-mutated glioblastoma. Increased angiogenesis as found here in the subset of patients with loss of *CDKN2A* may reflect the effects of the *CDKN2A* genetic locus that encodes two tumor suppressors that, among other functions, mediate antiangiogenic effects (32). Our voxel-based lesion symptom mapping analysis did not reproduce left temporal tumor location predilection for *MGMT*-methylated tumors as reported by Ellingson and colleagues (5,9)

(in a cohort of 433 glioblastoma), and we could also not confirm significantly higher contrast-enhancing or nonenhancing tumor volumes and higher ADCs (as previously reported in cohorts of 433 and 185 glioblastomas, respectively) for tumors with unmethylated *MGMT*. Thus, the suggestion of subtle yet significant associations between imaging characteristics and *MGMT* at previous studies requires further validation given the lack of such findings in our study to assert that these associations are of sufficient strength to enable clinically meaningful prediction of *MGMT* status outside of single-institution experiences.

Our data are derived from a homogeneous, single-institution cohort of patients with newly diagnosed glioblastoma and included comprehensive molecular and imaging characterization with robust quantitative analysis of high-quality imaging data, which overcomes methodic shortcomings of alternative user-dependent semi-quantitative or qualitative analysis. However, our study has limitations. First, class imbalances can potentially cause a negative effect on fitting of machine learning classification models and were present for several molecular parameters. Class imbalances were mitigated by using subsampling techniques that downsample the majority class and synthesize new data points in the minority class, which is recognized as a suitable approach in machine learning. Second, glioblastoma is a multiscale heterogeneous tumor varying both across patients as well as spatially within each single tumor. Thus, potentially different results may have been obtained in a cohort of patients subjected to image-guided stereotactic tissue sampling; we note, however, that even minimally invasive burr hole–based stereotactic procedures are associated with intraoperative brain shifts in the range of 0–10 mm (33) and are affected by sampling errors and the inability to sample the tumor comprehensively. Moreover, despite the presence of intratumoral heterogeneity (34), several studies found that the *MGMT*

Figure 2

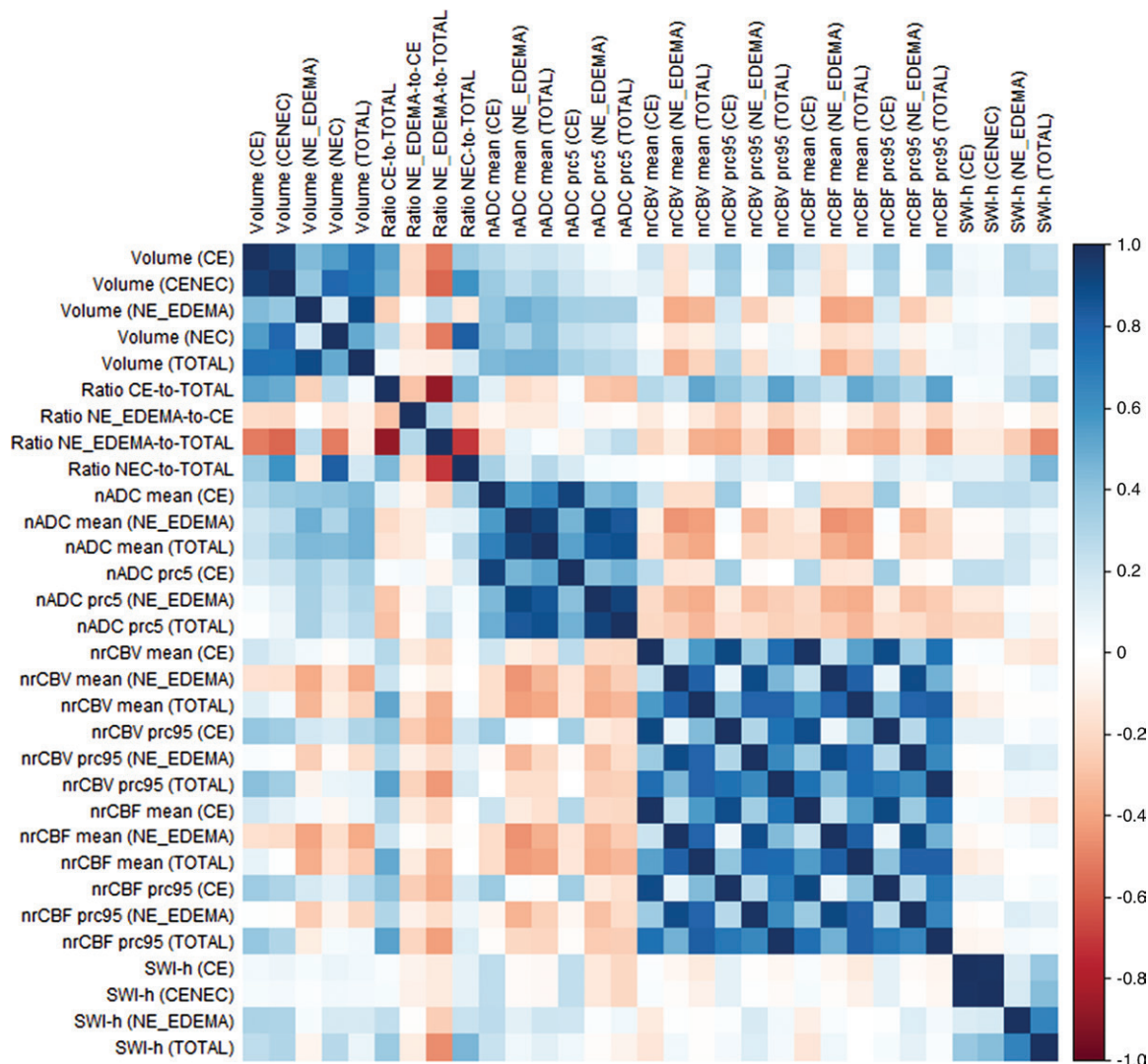


Figure 2: Pearson correlation matrix of evaluated MR imaging parameters. *CE* = contrast-enhancing tumor segmentation, *CENEC* = contrast-enhancing tumor plus necrosis segmentation, *NE_EDEMA* = nonenhancing FLAIR-hyperintense tumor segmentation, *NEC* = necrosis segmentation, *prc* = percentile, *SWI-h* = fraction of hypointense signals (percentage) on susceptibility-weighted images.

methylation level is relatively consistent throughout individual gliomas (35–38). Whether this homogeneity is a unique feature of *MGMT* or whether it is also applicable to the assessed CNVs and/or global DNA methylation subgroups remains to be investigated in future studies.

In summary, we found associations between established MR imaging parameters and molecular characteristics; however, they were not of sufficient strength to allow the generation of

machine learning classification models for reliable and clinically meaningful prediction of the assessed molecular characteristics in patients with newly diagnosed glioblastoma.

Acknowledgments: We thank the Genomics and Proteomics Core Facility of the German Cancer Research Center (DKFZ) for excellent technical assistance.

Complete list of authors: Philipp Kickingeder, MD, David Bonekamp, MD, Martha Nowosielski, MD, PhD, Annkathrin Kratz, MD, Martin Sill, PhD, Sina Burth, MD, Antje Wick,

MD, Oliver Eidel, MD, Heinz-Peter Schlemmer, MD, PhD, Alexander Radbruch, MD, Jürgen Debus, MD, PhD, Christel Herold-Mende, PhD, Andreas Unterberg, MD, David Jones, PhD, Stefan Pfister, MD, Wolfgang Wick, MD, Andreas von Deimling, MD, Martin Bendszus, MD, and David Capper, MD.

Author affiliations: Department of Neuroradiology, University of Heidelberg Medical Center, Im Neuenheimer Feld 400, 69120 Heidelberg, Germany (P.K., S.B., O.E., M.B.); German Cancer Research Center (DKFZ), Department of Radiology, Heidelberg, Germany (D.B., H.P.S., A.R.); Department of Neurology, Medical University Innsbruck, Austria (M.N.); Department of Neu-

ropathology, University of Heidelberg Medical Center, Heidelberg, Germany (A.K., A.v.D., D.C.); German Cancer Consortium (DKTK), Clinical Cooperation Unit Neuropathology, German Cancer Research Center (DKFZ), Heidelberg, Germany (A.K., A.v.D., D.C.); Division of Biostatistics, DKFZ, Heidelberg, Germany (M.S.); Neurology Clinic, University of Heidelberg Medical Center, Heidelberg, Germany (M.N., S.B., A.W., W.W.); Department of Radiation Oncology, University of Heidelberg Medical Center, Heidelberg, Germany (J.D.); Clinical Cooperation Unit Radiation Oncology, German Cancer Research Center (DKFZ), Heidelberg, Germany (J.D.); Division of Neurosurgical Research, Department of Neurosurgery, University of Heidelberg Medical Center, Heidelberg, Germany (C.H.M.); Department of Neurosurgery, University of Heidelberg Medical Center, Heidelberg, Germany (A.U.); Division of Pediatric Neurooncology, German Cancer Research Center (DKFZ), Heidelberg, Germany (D.J., S.P.); German Cancer Consortium (DKTK) Core Center Heidelberg, Heidelberg, Germany (D.J., S.P.); Department of Pediatric Oncology, Hematology and Immunology, Heidelberg University Hospital, Heidelberg, Germany (S.P.); and German Cancer Consortium (DKTK), Clinical Cooperation Unit Neurooncology, DKFZ, Heidelberg, Germany (W.W.).

Disclosures of Conflicts of Interest: P.K. disclosed no relevant relationships. D.B. disclosed no relevant relationships. M.N. disclosed no relevant relationships. A.K. disclosed no relevant relationships. M.S. disclosed no relevant relationships. S.B. disclosed no relevant relationships. A.W. disclosed no relevant relationships. O.E. disclosed no relevant relationships. H.P.S. Activities related to the present article: disclosed no relevant relationships. Activities not related to the present article: is a paid consultant for Curagita; receives payment for lectures including service on speakers bureaus from Siemens. Other relationships: disclosed no relevant relationships. A.R. Activities related to the present article: disclosed no relevant relationships. Activities not related to the present article: is a paid consultant for Bayer, Guerbet, GE Healthcare, and Bracco; institution has grants/grants pending from Guerbet; receives payment for lectures including service on speakers bureaus from Bayer, Guerbet, and Siemens; receives payment for development of educational presentations from Bayer, Guerbet, and Siemens; receives travel/accommodations/meeting expenses unrelated to activities listed from Bayer and Guerbet. Other relationships: disclosed no relevant relationships. J.D. disclosed no relevant relationships. C.H. disclosed no relevant relationships. A.U. disclosed no relevant relationships. D.J. Activities related to the present article: disclosed no relevant relationships. Activities not related to the present article: has grants/grants pending from Illumina. Other relationships: disclosed no relevant relationships. S.P. disclosed no relevant relationships. W.W. disclosed no relevant relationships. A.v.D. disclosed no relevant relationships. M.B. Activities related to the present article: disclosed no relevant rela-

tionships. Activities not related to the present article: received a grant from Novartis, Guerbet, DFG, Siemens, Stryker, and Medtronic; received personal fees from Novartis, Guerbet, Codman, Bayer, Teva, Vascular Dynamics, and Roche. Other relationships: disclosed no relevant relationships. D.C. Activities related to the present article: disclosed no relevant relationships. Activities not related to the present article: disclosed no relevant relationships. Other relationships: has a patent pending.

References

- Wen PY, Macdonald DR, Reardon DA, et al. Updated response assessment criteria for high-grade gliomas: response assessment in neuro-oncology working group. *J Clin Oncol* 2010;28(11):1963–1972.
- Ellingson BM, Bendszus M, Boxerman J, et al. Consensus recommendations for a standardized brain tumor imaging protocol in clinical trials. *Neuro Oncol* 2015;17(9):1188–1198.
- Diehn M, Nardini C, Wang DS, et al. Identification of noninvasive imaging surrogates for brain tumor gene-expression modules. *Proc Natl Acad Sci U S A* 2008;105(13):5213–5218.
- Mabray MC, Barajas RF Jr, Cha S. Modern brain tumor imaging. *Brain Tumor Res Treat* 2015;3(1):8–23.
- Ellingson BM. Radiogenomics and imaging phenotypes in glioblastoma: novel observations and correlation with molecular characteristics. *Curr Neurol Neurosci Rep* 2015; 15(1):506.
- Gevaert O, Mitchell LA, Achrol AS, et al. Glioblastoma multiforme: exploratory radiogenomic analysis by using quantitative image features. *Radiology* 2014;273(1):168–174.
- Zinn PO, Mahajan B, Sathyan P, et al. Radiogenomic mapping of edema/cellular invasion MRI-phenotypes in glioblastoma multiforme. *PLoS One* 2011;6(10):e25451.
- Pope WB. Genomics of brain tumor imaging. *Neuroimaging Clin N Am* 2015;25(1):105–119.
- Ellingson BM, Lai A, Harris RJ, et al. Probabilistic radiographic atlas of glioblastoma phenotypes. *AJNR Am J Neuroradiol* 2013;34(3):533–540.
- Naeini KM, Pope WB, Cloughesy TF, et al. Identifying the mesenchymal molecular subtype of glioblastoma using quantitative volumetric analysis of anatomic magnetic resonance images. *Neuro Oncol* 2013;15(5): 626–634.
- Gutman DA, Cooper LA, Hwang SN, et al. MR imaging predictors of molecular profile and survival: multi-institutional study of the TCGA glioblastoma data set. *Radiology* 2013; 267(2):560–569.
- Pope WB, Chen JH, Dong J, et al. Relationship between gene expression and enhancement in glioblastoma multiforme: exploratory DNA microarray analysis. *Radiology* 2008;249(1):268–277.
- Colen RR, Vangel M, Wang J, et al. Imaging genomic mapping of an invasive MRI phenotype predicts patient outcome and metabolic dysfunction: a TCGA glioma phenotype research group project. *BMC Med Genomics* 2014;7:30.
- Carlson MR, Pope WB, Horvath S, et al. Relationship between survival and edema in malignant gliomas: role of vascular endothelial growth factor and neuronal pentraxin 2. *Clin Cancer Res* 2007;13(9):2592–2598.
- Pope WB, Mirsadraei L, Lai A, et al. Differential gene expression in glioblastoma defined by ADC histogram analysis: relationship to extracellular matrix molecules and survival. *AJNR Am J Neuroradiol* 2012; 33(6):1059–1064.
- Itakura H, Achrol AS, Mitchell LA, et al. Magnetic resonance image features identify glioblastoma phenotypic subtypes with distinct molecular pathway activities. *Sci Transl Med* 2015;7(303):303ra138.
- Weller M, Cloughesy T, Perry JR, Wick W. Standards of care for treatment of recurrent glioblastoma: are we there yet? *Neuro Oncol* 2013;15(1):4–27.
- Kim H, Zheng S, Amini SS, et al. Whole-genome and multisector exome sequencing of primary and post-treatment glioblastoma reveals patterns of tumor evolution. *Genome Res* 2015;25(3):316–327.
- Hegi ME, Diserens AC, Gorlia T, et al. MGMT gene silencing and benefit from temozolomide in glioblastoma. *N Engl J Med* 2005;352(10):997–1003.
- Dunn GP, Rinne ML, Wykosky J, et al. Emerging insights into the molecular and cellular basis of glioblastoma. *Genes Dev* 2012; 26(8):756–784.
- Sturm D, Witt H, Hovestadt V, et al. Hotspot mutations in H3F3A and IDH1 define distinct epigenetic and biological subgroups of glioblastoma. *Cancer Cell* 2012;22(4): 425–437.
- Jones DT, Capper D, Sill M, et al. Next-generation neuropathology: improving diagnostic accuracy for brain tumors using DNA methylation array-based molecular profiling. *Neuro Oncol* 2014;16(Suppl 3):iii4.

23. Capper D, Jones DTW, Sill M, et al. DNA methylation array-based molecular profiling for brain tumor classification. Presented at the 60th annual meeting of the German Society for Neuropathology and Neuroanatomy (DGNN), Berlin, Germany, 2015.
24. Bady P, Sciuscio D, Diserens AC, et al. MGMT methylation analysis of glioblastoma on the Infinium methylation BeadChip identifies two distinct CpG regions associated with gene silencing and outcome, yielding a prediction model for comparisons across datasets, tumor grades, and CIMP-status. *Acta Neuropathol (Berl)* 2012;124(4):547–560. [Published correction appears in *Acta Neuropathol* 2013;126(1):159.]
25. Wiestler B, Capper D, Hovestadt V, et al. Assessing CpG island methylator phenotype, 1p/19q codeletion, and MGMT promoter methylation from epigenome-wide data in the biomarker cohort of the NOA-04 trial. *Neuro Oncol* 2014;16(12):1630–1638.
26. Kuhn M. Building predictive models in R using the caret package. *J Stat Softw* 2008;28(5):26.
27. Barajas RF Jr, Phillips JJ, Parvataneni R, et al. Regional variation in histopathologic features of tumor specimens from treatment-naïve glioblastoma correlates with anatomic and physiologic MR Imaging. *Neuro Oncol* 2012;14(7):942–954.
28. Eskilsson E, Rosland GV, Talasila KM, et al. EGFRvIII mutations can emerge as late and heterogenous events in glioblastoma development and promote angiogenesis through Src activation. *Neuro Oncol* doi: 10.1093/neuonc/nov113. Published online June 10, 2016. Accessed August 28, 2016.
29. Mellinghoff IK, Wang MY, Vivanco I, et al. Molecular determinants of the response of glioblastomas to EGFR kinase inhibitors. *N Engl J Med* 2005;353(19):2012–2024.
30. Aldape KD, Ballman K, Furth A, et al. Immunohistochemical detection of EGFRvIII in high malignancy grade astrocytomas and evaluation of prognostic significance. *J Neuropathol Exp Neurol* 2004;63(7):700–707.
31. Arevalo-Perez J, Thomas AA, Kaley T, et al. T1-weighted dynamic contrast-enhanced MRI as a noninvasive biomarker of epidermal growth factor receptor vIII status. *AJNR Am J Neuroradiol* 2015;36(12):2256–2261.
32. Zerrouqi A, Pyrzynska B, Febbraio M, Brat DJ, Van Meir EG. P14ARF inhibits human glioblastoma-induced angiogenesis by up-regulating the expression of TIMP3. *J Clin Invest* 2012;122(4):1283–1295.
33. Ivan ME, Yarlagadda J, Saxena AP, et al. Brain shift during bur hole-based procedures using interventional MRI. *J Neurosurg* 2014;121(1):149–160.
34. Patel AP, Tirosh I, Trombetta JJ, et al. Single-cell RNA-seq highlights intratumoral heterogeneity in primary glioblastoma. *Science* 2014;344(6190):1396–1401.
35. Hamilton MG, Roldán G, Magliocco A, McIntyre JB, Parney I, Easaw JC. Determination of the methylation status of MGMT in different regions within glioblastoma multiforme. *J Neurooncol* 2011;102(2):255–260.
36. Grasbon-Frodl EM, Kreth FW, Ruitter M, et al. Intratumoral homogeneity of MGMT promoter hypermethylation as demonstrated in serial stereotactic specimens from anaplastic astrocytomas and glioblastomas. *Int J Cancer* 2007;121(11):2458–2464.
37. Dunn J, Baborie A, Alam F, et al. Extent of MGMT promoter methylation correlates with outcome in glioblastomas given temozolomide and radiotherapy. *Br J Cancer* 2009;101(1):124–131.
38. van Thuijl HF, Mazon T, Johnson BE, et al. Evolution of DNA repair defects during malignant progression of low-grade gliomas after temozolomide treatment. *Acta Neuropathol (Berl)* 2015;129(4):597–607.